JOURNAL OF GEOPHYSICAL RESEARCH, VOL. 111, A09220, doi:10.1029/2006JA011730, 2006

Characteristics of Jovian morning bright FUV aurora from Hubble Space Telescope/Space Telescope Imaging Spectrograph imaging and spectral observations

J. Gustin,[1] S. W. H. Cowley,[2] J.-C. Gérard,[1] G. R. Gladstone,[3] D. Grodent,[1] and J. T. Clarke[4]

Received 21 March 2006; revised 31 May 2006; accepted 8 June 2006; published 28 September 2006.

[1] Observation of an exceptionally bright (peaking at ~1.8 MR) Jovian auroral morning arc was obtained with the Space Telescope Imaging Spectrograph (STIS) on 21 September 1999, both in the imaging and spectral modes. The images of the HST orbit are used to describe the variation of the position of the bright arc, while the time-tagged spectra are examined to derive the properties of the precipitating auroral electrons, such as their mean energy and the electron current density at the top of the atmosphere. The first and the last images of the HST orbit, separated by 37 min, show that the bright morning emission is situated on the reference oval, with a ''leading'' edge fixed in λ_{III} longitudes (i.e., rotating with the planet), and a ''trailing'' edge that extends into the nightside. The auroral arc is divided in two branches, as was also observed in some previous analyses. An isolated bright spot is also observed at λ_{III} ~184°. Its brightness reaches 500 kR and it also approximately corotates with Jupiter. Four regions of the auroral morning arc captured by the STIS aperture were extracted from the spectral observation. The four associated low-resolution spectra (~4.8 Å) show very different characteristics. In particular, two spectra reveal unusually high color ratios (18.5 and 45.5), with corresponding mean electron energies of ~280 and ~460 keV, respectively. The current densities associated with three of the spectra lie in the range 0.09–0.2 $\mu A\ m^{-2}$, consistent with previous estimates, while the fourth spectrum is characterized by a mean current density of 0.54 $\mu A\ m^{-2}$, outside the range ~0.04–0.4 $\mu A\ m^{-2}$ obtained in a previous study of G140L spectra of the Jovian main oval. Assuming that main oval aurorae are caused by field-aligned electric fields, the relationship between the energy flux and the current density derived from the spectra has been compared to the Knight's theory of field-aligned currents. Because of the very high acceleration potential derived from two of the extracted spectra, a relativistic treatment of the Knight theory was used. Assuming an electron temperature T_e = 2.5 keV, it is seen that the two regions corresponding to earlier local times (higher λ_{III} longitudes) reveal an electron source density lower than the values observed in the equatorial plane during the Voyager flybys. On the other hand, the equatorward region (lowest latitude) exhibits an electron source density in the upper range of usual values. Analysis of time-tag spectra reveals that the variations of the energy flux and the color ratios are large but continuous and generally covary.

Citation: Gustin, J., S. W. H. Cowley, J.-C. Gérard, G. R. Gladstone, D. Grodent, and J. T. Clarke (2006), Characteristics of Jovian morning bright FUV aurora from Hubble Space Telescope/Space Telescope Imaging Spectrograph imaging and spectral observations, *J. Geophys. Res.*, *111*, A09220, doi:10.1029/2006JA011730.

1. Introduction

[2] The Jovian aurora is the most powerful auroral energy source in the solar system, depositing between 10^{13} and 10^{14} W into each polar region. The Jovian ultraviolet (UV) aurora was first observed with the UV spectrometer on board the Voyager 1 and 2 spacecraft in 1979 [*Broadfoot et al.*, 1979]. The Voyager UVS experiment detected emission from the H Lyman-α and the H_2 Lyman ($B^1\ \Sigma_g^+ \rightarrow X^1\ \Sigma_g^+$) and Werner ($C^1\ \Pi_u^+ \rightarrow X^1\ \Sigma_g^+$) system bands between 875 and 1500 Å. The International Ultraviolet Explorer (IUE) spectrograph extended the spectral coverage up to 1700 Å. *Yung et al.* [1982] compared the IUE observations between

[1]Laboratoire de Physique Atmosphérique et Planétaire, Université de Liège, Liège, Belgium.
[2]Department of Physics and Astronomy, University of Leicester, Leicester, UK.
[3]Space Science Department, Southwest Research Institute, San Antonio, Texas, USA.
[4]Center for Space Physics, Boston University, Boston, Massachusetts, USA.

0148-0227/06/2006JA011730$09.00

1200 and 1700 Å with synthetic spectra and established that below 1400 Å H_2 auroral emission is attenuated by methane and other hydrocarbons that overly the auroral emission region. They introduced the concept of the color ratio $CR = I(1550-1620Å)/I(1230-1300Å)$, which is related to the altitude of the emission and has been used as an indicator of the penetration depth of the electrons in the atmosphere relative to the hydrocarbon homopause. Its value is equal to 1.1 for an unabsorbed spectrum and rises as the precipitating electron mean energy increases.

[3] Observations obtained with successive cameras on the Hubble Space Telescope (HST) have shown a complex and dynamical auroral structure. They revealed that the auroral morphology is characterized by (1) a main oval which maps magnetically in the magnetosphere beyond 20 Jovian radius (R_J), (2) scattered diffuse emission poleward of the main oval showing large variations on timescales of minutes, and (3) flux tube footprint emissions of the moons Io, Europa, and Ganymede [*Gérard et al.*, 1994; *Ballester et al.*, 1996; *Prangé et al.*, 1998; *Grodent et al.*, 2006; *Clarke et al.*, 1996, 1998, 2002]. This paper is concerned with phenomena associated with the main oval emissions. Owing to its more favorable viewing geometry, most studies of Jupiter's auroras have concentrated on the northern polar region. Here the oval is observed to have a distinctly noncircular shape, with auroras of differing character occurring in differing regions around the oval [e.g., *Grodent et al.*, 2003a]. The main oval structure is observed to near-rigidly corotate with the planet (at least over that portion of the jovian rotation when the auroras can be well observed from Earth), suggesting that it is controlled by the rigidly rotating form of the planetary magnetic field. The shape of the oval, and the nature of the auroras around it, can thus be described in terms of System III longitude. Generally, the northern oval takes the form of a narrow bright arc for System III longitudes greater than $\lambda_{III} \sim 180°$, and of broader, more structured, emissions for longitudes less than $\lambda_{III} \sim 180°$. When the magnetic axis is tilted toward the Earth such that viewing is at its best (thus corresponding to a large number of observations), the former narrower emission is located in the dawn sector, while the latter broader emission is located in the dusk sector.

[4] On a small number of occasions, the intensity of the narrow arc emission which is generally seen in the dawn sector has been observed to be significantly enhanced. The first such observations were obtained on 17 July 1993 with the HST Faint Object Camera (FOC), which revealed the transient presence of a remarkably intense and discrete arc, extending from the dawn into the morning sector [*Gérard et al.*, 1994]. This observation was characterized by an apparent emission rate of ~6 mega-Rayleigh (1 MR = 10^{12} photons per cm^2 per sec over 4π steradians) of total H_2 Lyman and Werner band emission. This bright arc lay close to magnetic field lines mapping into the equatorial plane at about 30 R_J, according to the GSFC 06 magnetic model [*Connerney*, 1992]. The leading edge of the bright emission was located near System III longitude $\lambda_{III} = 180°$ and remained fixed in System III longitude as the planet rotated.

[5] *Ballester et al.* [1996] identified another bright event near the dawn limb in images obtained on 31 May 1994 with the Wide Field Planetary Camera 2 (WFPC2). The auroral emission started at the latitude of the main oval and expanded longitudinally and equatorward, mapping out to a width of several R_J in the middle and inner magnetosphere. The auroral intensity increased by a factor of ~9 in 1.8 hours, peaking at ~3 MR, corresponding to at least 420 mW m^{-2} of local energy input. They pointed out that such a large energy input could alter the CH_4 absorption of the auroral photons below 1400 Å, due to upwelling of additional CH_4 from deeper layers. *Ballester et al.* [1996] also found evidence for a lag from rigid corotation of the bright emission region, estimated to be as much as ~30%.

[6] *Clarke et al.* [1998] compared these bright emissions, together with a third observed by the WFPC2 on 23 June 1996 and showed that all three lay along the reference oval with a resolved but narrow latitudinal width, extending from the dawn limb in each case to differing distances along the oval. This connection with dawn led *Clarke et al.* [1998] to call these remarkable events "dawn storms," with the possible implication of a solar wind local time influence. However, for the 31 May 1994 event, *Ballester et al.* [1996] did not find any solar wind correlation based on data measured at Earth and by the Galileo orbiter.

[7] FUV images of the polar aurora obtained with the Space Telescope Imaging Spectrograph (STIS) on 16 December 2000 showed a complex morphology, consisting of parallel bright arcs located at the poleward edge of the morningside main oval [*Grodent et al.*, 2003b]. These emissions, labeled as "multiple dawn arcs" (MDA) by *Grodent et al.* [2003b], appear to corotate with Jupiter.

[8] In a more general way, STIS FUV observations of the polar aurora have provided a global view of the Jovian aurora with unprecedented spatial, temporal [*Clarke et al.*, 1998, 2002; *Waite et al.*, 2001; *Grodent et al.*, 2003a, 2003b], and spectral [*Gustin et al.*, 2002; *Gérard et al.*, 2002, 2003] resolution. Results from STIS images showed that the main oval maps magnetically to distances outside Ganymede's orbit (15 R_J) [*Clarke et al.*, 2002], a region where the flow of plasma increasingly departs from rigid corotation. A model of corotation-related currents developed by *Hill* [1979, 1980] was combined by *Cowley and Bunce* [2001] with *Knight*'s [1973] kinetic theory of auroral acceleration by field-aligned electric fields to show that field-aligned potential drops of ~50–150 kV are required to drive the upward currents associated with discrete auroral emissions. This picture was confirmed by *Gustin et al.* [2004], who analyzed 23 spectra obtained with STIS between July 1997 and January 2001. Through the relationship between the flux and the mean energy of the precipitated primary electrons obtained with Knight's formulation, they showed in a mean energy versus energy flux diagram that data points were bracketed by Knight curves, with an electron temperature of ~2.5 keV and an equatorial source density ranging between 0.001 and 0.01 cm^{-3}, that is within values observed in the equatorial plane during the Voyager flybys [*Scudder et al.*, 1981]. Extensive studies of the STIS and GHRS (Goddard High Resolution Spectrograph) spectral database have permitted an estimation of the precipitating electron mean energy of 30 to 210 keV for the main oval, 50 to 150 keV for the polar regions, and about 50 keV for the Io footprint and tail [*Dols et al.*, 2000; *Gustin et al.*, 2002, 2004; *Gérard et al.*, 2002, 2003].

[9] In this paper we perform a detailed analysis of a Jovian bright dawn auroral event which appears to have

Table 1. Characteristics of the STIS Exposures Obtained on 21 September 1999

Filename	Start, UT	Exposure, s	Mode	Filter/Grating	CML,[a] deg
o5hya4icq	2201:00	300	Timetag	SrF	179.6
o5hya4ieq	2212:00	113	Accum	Clear	185.4
o5hya4igq[b]	2219:00	800	Timetag	G140L	192.6
o5hya4iiq	2238:00	400	Timetag	SrF	204.4

[a]At midexposure.
[b]In the spectral mode, the 1024 × 1024 MAMA detector provides 1024 spatially resolved spectra [see *Gustin et al.*, 2002]. To avoid confusion, the observation in the spectral mode is called a ''spectral observation,'' while individual spectra extracted from the MAMA detector are simply called ''spectrum'' or ''spectra.''

much in common with the three events discussed above, which was observed with STIS in September 1999 for the first time, both in the imaging and spectral modes. We first describe the variations of the position of the morning arc on the planet and use the results to define this remarkable observation. The temporal variations and time-integrated spectra are then examined to derive the properties of the primary electrons producing such an event. Finally, we make the assumption that this event is produced by electrons accelerated by field-aligned electric fields in regions of upward directed field-aligned current, and examine the consequences for its origins that follow.

2. Spatial Characteristics of the Morning Bright Event

2.1. Auroral Images

[10] Three images and a spectral observation were obtained with STIS during the HST orbit of 21 September 1999, between 2201:00 and 2244:30 UT (Table 1). The images can be used to locate the bright event within the north polar region of Jupiter and to characterize its spatial and temporal brightness variations. Figure 1 shows the position of the bright arc on the first (Figure 1a) and last (Figure 1b) images obtained during the HST orbit. Both images were obtained with the strontium-fluoride (SRF2) filter, which blocks off the Lyman-α emission and other emissions below 1300 Å. As part of the reduction process, the images were flat-fielded and corrected for geometric distortions and dark counts [*Grodent et al.*, 2003a, 2003b]. Signals from the MultiAnode Micro channel Array (MAMA) detector of STIS were converted into flux units using a factor of 1.5 counts per pixel per second for 1 MR of H_2 plus Lyman-α (which contributes ~15% of the total auroral emission between 1100 and 1700 Å).

[11] Through a procedure described by *Grodent et al.* [2003b], the images were projected onto a System III map, that is, each pixel of the initial image is assigned a planetocentric latitude and a λ_{III} longitude. In this projection, features corotating with the planet appear at a fixed location. Furthermore, any features leading (lagging) corotation move anticlockwise (clockwise), i.e., to lower (larger) λ_{III} longitude, from one projected image to the next and can therefore be easily identified. Note that the terms ''leading'' and ''trailing'' employed hereafter refer to the direction of motion with respect to the planet's rotation.

2.2. Spatial and Temporal Properties of the Morning Arc

[12] The images at the start (Figure 1a) and at the end (Figure 1b) of the HST orbit are separated by 37 min, corresponding to a Jovian rotation angle of 21°. On the polar projections, the reference oval defined by *Grodent et al.* [2003b], obtained from FUV images, is overplotted in red on each panel. They estimate that during normal conditions, the brightness of the main oval varies from ~50 to ~500 kR, and hence in Figure 1 we arbitrarily choose to saturate in white any regions brighter than 500 kR. It is seen that the bright dawn emissions are located on the reference oval, with λ_{III} longitudes ranging from ~195° to ~245° for the first image and from ~200° to ~260° for the last (green arcs on the inner white circle of Figure 1, with λ_{III} longitudes rounded to the nearest 5°). The leading edge of the dawn arc is thus close to be fixed in λ_{III} longitude (i.e., it rotated with the planet), near to the location where the character of the main oval emissions changes from narrow and arc-like to broader and more structured as discussed in section 1 above, and as can be seen directly in Figure 1. There is actually a ~5° difference between the leading edge's λ_{III} longitude in the first and last images, which corresponds to a corotation lag ~25%. This value is somewhat approximate, since the short time interval between the first and last images gives a high relative longitude uncertainty. Also, the position of the trailing edge's limit is visually determined, yielding a ~1° uncertainty. Near-corotation also applied to the bright emission reported by *Gérard et al.* [1994], while the bright events reported by *Ballester et al.* [1996] and *Clarke et al.* [1998] did not extend along the narrow oval from dawn to such low values of the System III longitude. The ''trailing'' edge of the present event can also be seen to extend into the nightside between the first and last image, unlike the previous events where the emission was truncated at the dawn limb. The maximum brightnesses observed were ~1.1 and ~1.8 MR of total emission for the first and last images, respectively. For comparison, the brightness of the Io footprint on the last image, located at 52°N, λ_{III} = 177°, has a mean value of 200 kR (labeled IFT on Figure 1). An isolated bright spot is also observed at λ_{III}~185°, near the leading edge of the bright arc (marked with a green segment on Figure 1). This has a maximum brightness of ~500 kR, and also approximately corotates with the planet.

[13] From the λ_{III} longitudes, the magnetic local time (MLT) of each pixel was determined from the field line mapping to the equatorial plane. As mentioned previously, the main auroral oval is known to map to distances between 20 and 30 R_J in the Jovian magnetosphere. We used the VIP4 magnetic field model (Table 4 from *Connerney et al.* [1998]), to trace the field lines from a point on the planet to the magnetic equator at a radial distance of 30 R_J. Assuming that the CML corresponds to a local time of 1200, one may derive the MLT at 30 R_J. In the first image, the λ_{III} longitudes of the magnetic field lines of the bright arc range from ~230° to ~292° at 30 R_J and correspond to MLT from ~0430 to ~0840 (yellow segment in the outer circle of Figure 1a). Likewise, the magnetic longitude at 30 R_J corresponding to the enhanced region in the second image varies from 235° to 313°, leading to MLT from 0205 to ~0715 (yellow segment in the outer circle of Figure 1b). It

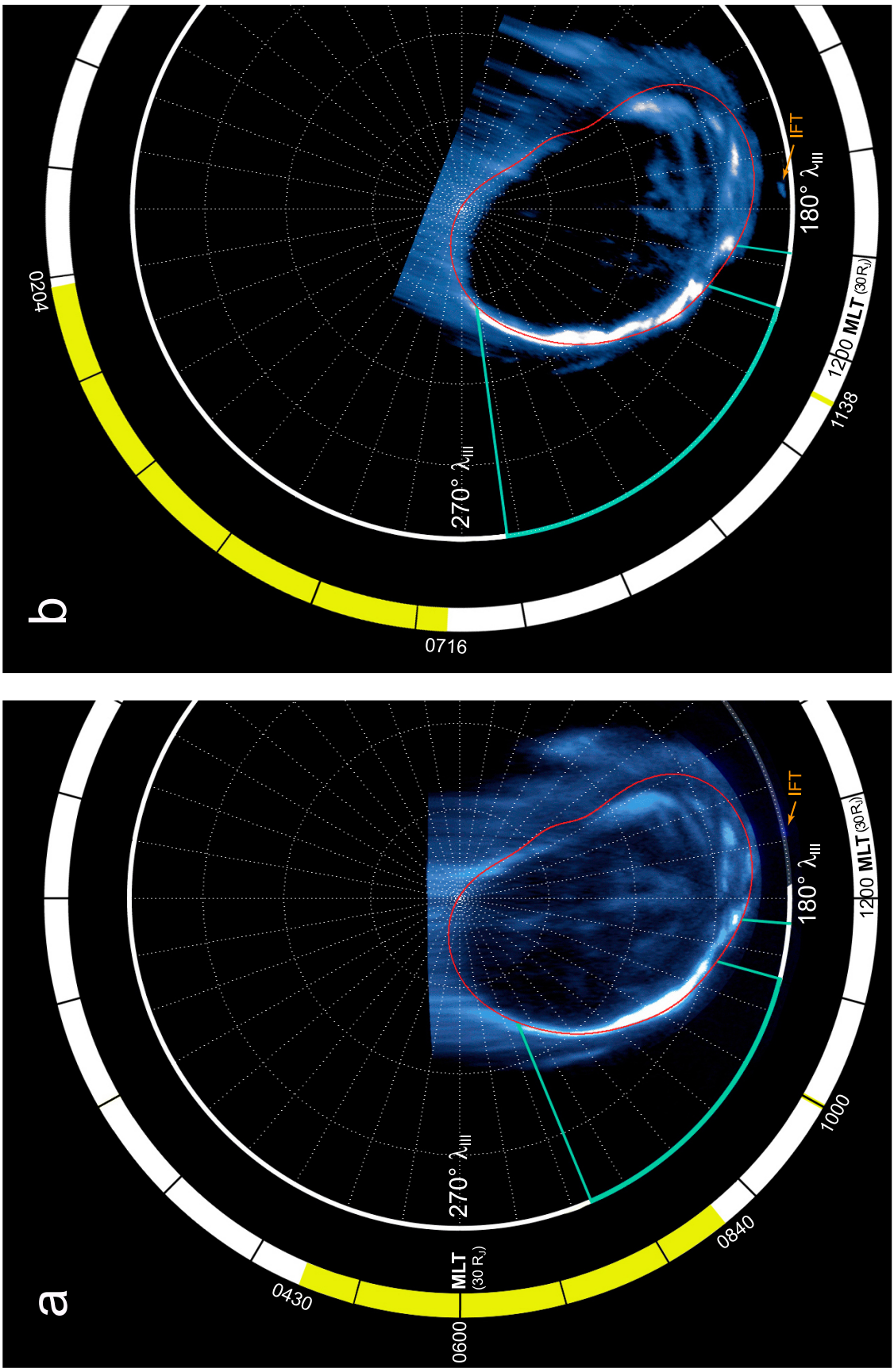

Figure 1. Polar projection of the bright morning arc on the first (a) and last (b) images of the HST orbit. The green segment on the inner circle shows the arc extension in λ_{III} coordinates and the yellow segment on the outer circle represents the local time of the corresponding magnetic field lines crossing the magnetic equator at radial distance of 30 R_J. The reference oval is indicated by the red line.

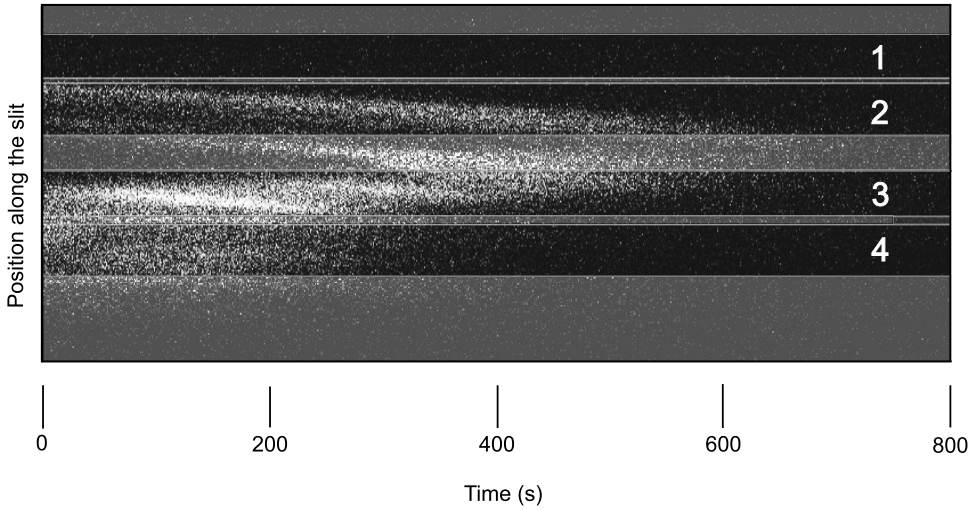

Figure 2. Time-tag sequence of the G140L spectrum, where each photon event on the MAMA detector in the unabsorbed spectral region above 1500 Å is represented as an individual point. The dark areas represent the regions selected for extraction of the four spectra from the observation.

should be noted that the considerable ''sweepback'' of the field lines (the difference between their equatorial and ionospheric longitudes) in the VIP4 model is entirely due to the nondipole terms in the equatorial current sheet. It means that the different amount of ''sweepback'' between Figures 1a and 1b cannot be attributed to the observed strengthening of the auroral current system. The MLT of the single bright spot varies from 1000 to 1140 between the two images.

[14] The bright event described here is comparable to the FOC observations reported by *Gérard et al.* [1994]. Its corotation with Jupiter makes it different from the bright dawn aurora described by *Ballester et al.* [1996], and its position on the reference oval distinguishes it from the MDA described by *Grodent et al.* [2003b], which were corotating dawn multiple parallel arcs, located poleward of the main oval.

3. Spectral Analysis

[15] We examine here the spectral observation obtained with the G140L grating, using the 25×0.2 arcsec^2 slit. The 1024×1024 pixels of the MAMA detector provide a series of spectra from 1150 to 1750 Å with ~4.8 Å resolution in the dispersion direction, and a uniform sampling in the spatial direction. STIS was operated in the TIMETAG mode for this observation, providing data in an event table containing separate columns for the pixel coordinates and the arrival time of each detected photon event, with an integration period of 125 μs.

3.1. Data Processing

[16] The temporal and spatial properties of the spectral observation are contained in a ''tag'' file, which provides the arrival time of individual photons on the detector. Figure 2 shows the auroral photons of the ''o5hya4igq_tag'' file, collected along the slit as a function of time. The spatial location of the photons along the slit and the time variations during the exposure are used to define the spatial and temporal zones where spectra are extracted. We have chosen four spatial regions, labeled 1 to 4 in Figure 2, corresponding to apparently coherent structures which maintain approximately the same spatial location during the exposure. Most of the auroral signal is obtained during the first half of the exposure. We thus initially extract and examine four spectra from the time-tag file, consisting of the first 440 s of the exposure for spatial regions 1, 2, and 3, and to the first 200 s for region 4 (see Figure 2). Results at higher (20 s) time resolution will also be shown below in section 3.5. The effect of the planet's rotation is readily apparent when looking at Figure 2. Notably, the downward slope of the groups of points observed in the plot is likely due to corotation of fixed features drifting through the slit. As for previous cases of temporal variations in the main oval region [*Gustin et al.*, 2004], the brightness variations are continuous and do not show rapid bursts over ~50–100 s, which are more typical of the high-latitude regions [*Gérard et al.*, 2003].

[17] Processing of these spectra includes dark and background subtractions, corrections for detector sensitivity, and conversion of the count rate into physical units of kilo-Rayleigh (kR). A detailed description of the methodology may be found in the work of *Gustin et al.* [2002, 2004].

3.2. Spectral Properties

[18] The processed spectra extracted over the spatial and temporal windows described above are displayed in Figure 3. An unabsorbed synthetic H_2 spectrum is shown by the dashed line along with spectrum 3 for comparison. Some differences are readily apparent in the brightness and degree of short-wavelength absorption. The emission at short wavelengths in regions 1 and 4 exhibits modest absorption, indicative of moderate values of the CR, comparable to typical values found in the literature ranging from 2 to 5 [*Dols et al.*, 2000; *Gérard et al.*, 2002; *Gustin et al.*, 2004]. Region 1 corresponds to the fainter aurora captured in the slit, while region 4 contains the brightest observed spectrum in the dataset. Regions 2 and 3, on the other hand, yield the largest CR values ever measured for Jupiter's aurora, with values of 18.5 and 45.5 for the 440 s averaged spectra. When averaged over shorter 20 s intervals, even larger maximum values of ~30 and ~62 are found in the two regions, as will

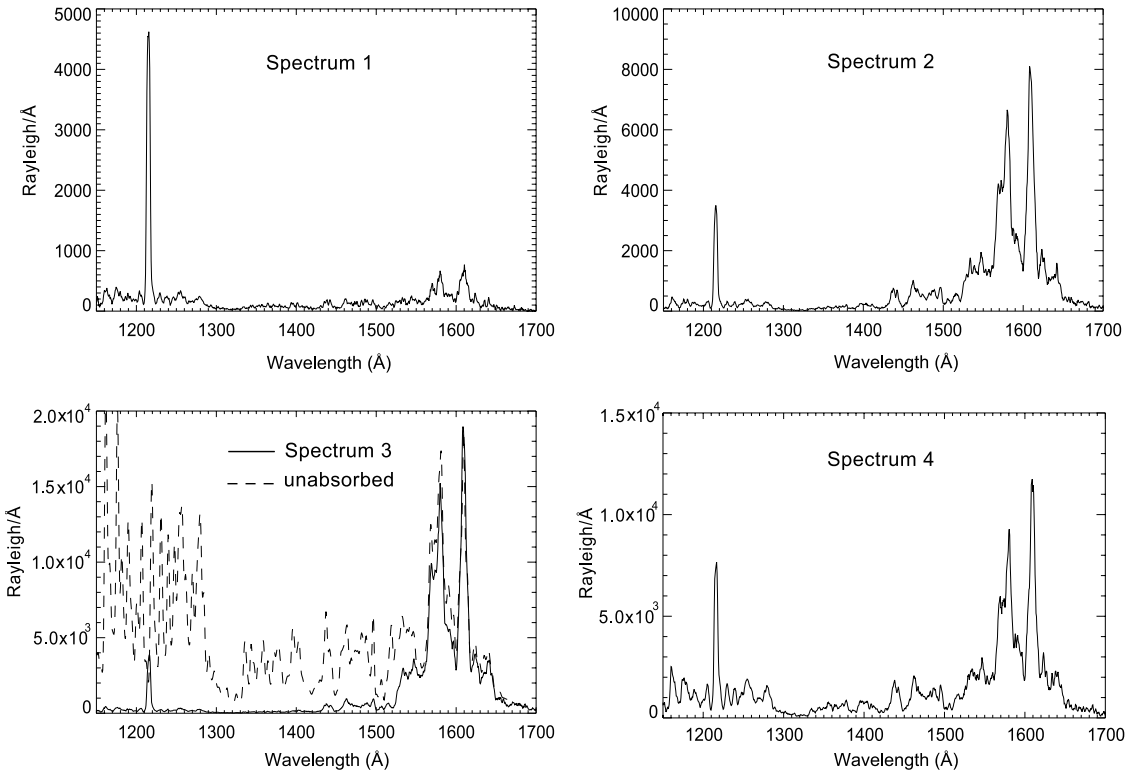

Figure 3. Extracted spectra obtained from the time-tag observation. Each spectrum corresponds to a fixed spatial location on the STIS G140L aperture, as shown in Figure 2. Spectra 2 and 3 are characterized by the highest color ratio ever observed over decades of auroral observations of Jupiter. A synthetic unabsorbed H_2 spectrum is overplotted in spectrum 3 for comparison.

be shown in the following section. Some important characteristics of the spectra are summarized in Table 2, including the brightness and the color ratio, where we show both mean values obtained from the above extended averaging intervals, and maximum values from the 20 s integrations.

3.3. Geometry of the Observations

[19] To visualize the approximate location of the G140L slit during the spectrum acquisition, we use the second STIS image of the HST orbit, obtained approximately 7 min before the spectral observation. Figure 4 shows the projection of the slit on the zoomed raw image, as indicated by the two vertical lines. As described by *Gustin et al.* [2002, 2004], the precise location of the G140L slit on the image is obtained by comparing the intensity distribution of the spectrum along the slit with a series of summed columns of the images corresponding to the width of the STIS slit. Comparison with Figure 1 shows that the STIS aperture lay along the main part of the brightened oval in the dawn sector, with a mean view angle of 64°. The regions corresponding to the four extracted spectra are represented in Figure 4 by the rectangular boxes, each marked with the corresponding latitude θ and λ_{III} longitude. It is also notable that the oval is split into two main branches, as has also been observed in a few other cases [*Grodent et al.*, 2003a, 2003b; *Gustin et al.*, 2004]. Spatial regions 1 and 2 view the homogeneous auroral arc corresponding to the poleward branch, while regions 3 and 4 lie in the multiple arc region, with region 3 being centered on the poleward branch, and region 4 on the equatorward branch.

Table 2. Characteristics of the Extracted Spectra

Extracted Spectrum	Duration, s	Max Brightness,[a] kR	Mean Brightness,[a] kR	Mean CR	Max CR	⟨E⟩,[b] keV	Mean Energy Flux $W_{\parallel}$,[c] mW m^{-2}	Mean Current Density $j_{\parallel}$, μA m^{-2}	Accelerating Voltage,[d] kV	Electron Source Density, m^{-3}
1	440	58	47	1.9	2.5	54	4.7	0.09	51.5	4800
2	440	475	429	18.5	29.9	277	42.9	0.16	274.5	880
3	440	1082	904	45.5	61.9	460	90.4	0.20	457.5	570
4	200	670	627	4.9	6.3	119	62.7	0.54	116.5	6900

[a]Total H_2 unabsorbed intensity in the [1140–1700 Å] window, converted to vertical value.
[b]Based on the procedure developed in section 3.
[c]Based on the vertical value of the mean brightness.
[d]Assumes a mean energy of 2.5 KV for the source electrons in the equatorial plan.

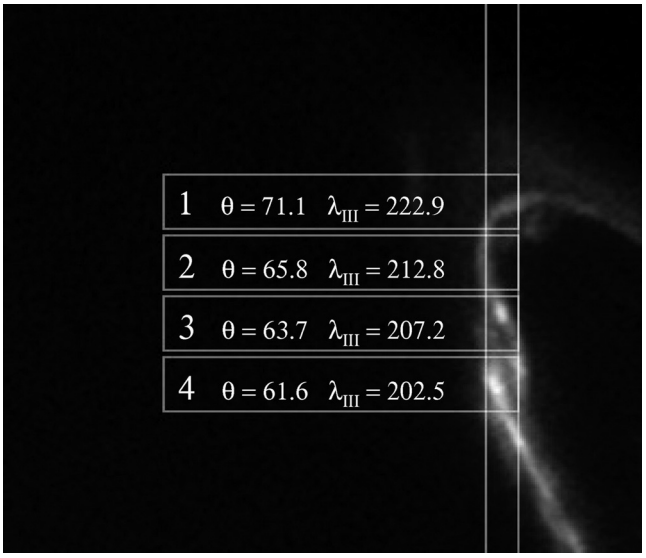

Figure 4. Position of the G140L 52″ X 0.2″ slit used to obtain spatially resolved spectra (marked by the double vertical line) overlaid on the (zoomed) image obtained 7 min before the spectral observation. The four rectangles correspond to the regions of the planet that were extracted. The latitudes θ and λ_{III} longitudes of the four spatial regions are also indicated.

3.4. Energy of the Primary Auroral Electrons

[20] As indicated above, the energy of the primary electrons that produce the auroral emission can be estimated from the hydrocarbon absorption observed in the FUV spectra, thus providing important information on the physical conditions occurring in the event. It is usually assumed that CH_4 and C_2H_2 are the main hydrocarbons that attenuate the auroral emission. Methane has a continuous absorption cross section below 1350 Å, while C_2H_2 has strong absorption peaks at 1480 and 1520 Å. As mentioned earlier, the CR is defined as the intensity ratio between the unabsorbed 1550–1620 Å spectral region and the absorbed 1230–1300 Å section of the spectrum. It is therefore a measure of the absorption of the H_2 auroral emission by hydrocarbons located within and above the region of auroral energy deposition. It is thus related to the depth of the peak auroral photon production and provides an indirect measurement of the energy of the precipitated electrons in the Jovian atmosphere. The model atmosphere used to derive a relationship between the CR and the energy of the precipitating electrons was described in detail by *Grodent et al.* [2001]. This model couples a two-stream electron transport model of energy deposition with a one-dimensional thermal conduction model including thermal cooling to calculate a self-consistent thermal structure adapted to the auroral upper atmosphere. In the version used for this study, the neutral atmosphere is taken from *Gladstone et al.*'s [1996] NEB model. The gravity acceleration is adapted to a latitude of 60° N. A Maxwellian initial energy spectrum is assumed for the auroral electrons at the top of the atmosphere with characteristic energy as a free parameter, leaving the methane vertical distribution unchanged. The atmosphere is vertically divided into 200 layers with equal pressure spacing. An H_2 spectrum is generated in each layer based on the local electron flux energy distribution, H_2 density, and temperature. The emerging spectrum for an Earth observer is obtained in physical units for any location and view angle by integrating the volume emission rate of each line or continuum interval along the line of sight, after attenuation by methane. A relationship between the CR and the mean electron energy was derived from a series of initial electron energy distributions. As stated in previous works [*Gérard et al.*, 2003; *Gustin et al.*, 2004], a unambigous relationship between the CR and the mean electron energy assumes that the homopause location is known. In this scheme, the eddy diffusion coefficient was set to 1.4×10^6 cm^2 s^{-1}, as in the work of *Grodent et al.* [2001]. This procedure applies to precipitating electrons with mean energies up to ~400 keV, giving CR values up to ~35. However, the 440 s averaged spectrum 3 is characterized by a CR of 45.5, peaking at 61.9 when averaged over 20 s intervals. The mean energies related to CR higher than 35 were obtained from second-order extrapolation of the CR–mean energy relationship. It should be noted that the high observed CR values argue for an auroral emission located far below the standard pressure level of 1×10^{-6} bar obtained from previous studies. It is thus reasonable to assume that other hydrocarbons than methane attenuate the H_2 auroral emission we observe. The mean electron energy we derive likely overestimates the true mean electron energy. On the basis of fits of spectrum 3 including the main hydrocarbons situated above the 1×10^{-6} bar pressure level, simulations of their effects will be included in a forthcoming paper. It is found from this procedure that for region 2 with a mean CR of 18.5 the energy of the primary electrons is 277 keV, while for region 3 with a mean CR of 45.5 the electron energy is 460 keV. The precipitating electron energies obtained from the averaged spectra from all four regions are given in Table 2, showing that the values for regions 1 and 4 are much lower, with values of 54 and 119 keV, respectively. The table also gives the mean precipitating electron energy flux obtained from these calculations, obtained from the vertical value of the mean brightness. If we then divide this by the energy of the primary electrons, we obtain the electron number flux, which multiplied by the electron charge gives the current density carried along the field lines by the auroral electrons at the top of the atmosphere. The values so obtained are ~0.1 μA m^{-2} for region 1, ~0.16 μA m^{-2} for regions 2, ~0.2 μA m^{-2} for region 3, and a larger value of ~0.54 μA m^{-2} for region 4. These values are also given in Table 2.

3.5. Time Variations

[21] As indicated above, the spectra we analyze were obtained in time-tag mode, which allows an examination of the temporal variations of the electron energy flux, color ratio, precipitating electron energy, and electron current density, for each of the four spatial regions employed over the 800 s observation. The results are shown in Figure 5, where the photon events have been integrated over 20 s intervals to provide a good signal-to-noise ratio while keeping sufficient time resolution. As mentioned by *Gustin et al.* [2004], changes during the spectral exposure may represent real time variations or may be caused by a brighter/fainter segment of the oval moving into the slit with the planetary rotation. The term "time variations" used

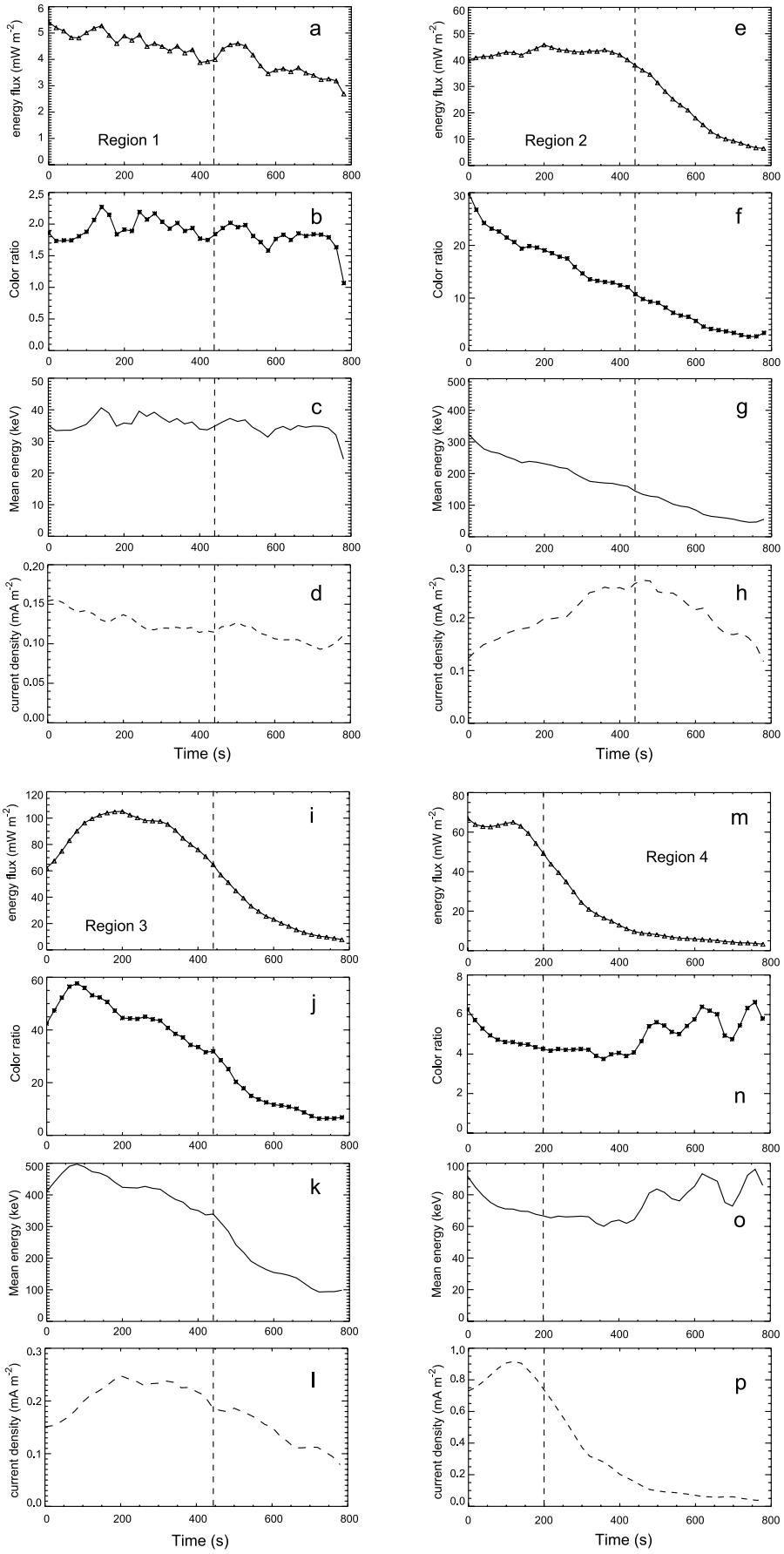
a
Region 1
energy flux (mW m-2)
b
Color ratio
c
Mean energy (keV)
d
current density (mA m-2)
Time (s)
e
Region 2
f
g
h
i
Region 3
j
k
l
m
Region 4
n
o
p

Figure 5

in this study thus refers to changes observed inside the STIS aperture during the time-tag sequence, independent of whether they are due to temporal or spatial effects.

3.5.1. Region 1

[22] The left panel of Figure 5a shows the time-tagged sequence for region 1. The 440 s interval to the left of the dashed vertical line represents the interval over which the averaged spectrum was obtained, shown in Figure 3 (as also shown in the other panels of the figure). The overall trend of the energy flux is a constant decrease, with values from $\sim$5.4 mW m^{-2} at the start to $\sim$2.7 mW m^{-2} at the end of the exposure. It corresponds to the fainter part of the aurora, with energy fluxes which are 10 times lower than the other auroral regions captured by the G140L slit. The values of the energy flux with time are therefore rather noisy. For example, a flux of 5 mW m^{-2} corresponds to $\sim$0.13 raw counts per pixel per second from photons in the 1500–1700 Å spectral region. Hence the corresponding CR during the sequence is also very noisy, since it combines the 1550–1620 Å unabsorbed spectral region and the 1230–1300 Å absorbed spectral region, which is in the fainter part of the entire UV spectrum. The CR slightly but continuously decreases with time, with values around 1.9, which corresponds to precipitating electrons with mean energies of $\sim$55 keV. Likewise, the mean energy slightly decreases during the sequence, with values that are well within the range of previous observations [*Dols et al.*, 2000; *Gustin et al.*, 2002, 2004; *Gérard et al.*, 2003, 2004]. The associated current density varies from $\sim$0.11 to 0.06 μA m^{-2}, which is reasonably typical of the values calculated from previous observations of main oval emissions [*Gustin et al.*, 2004].

3.5.2. Region 2

[23] Figure 5e shows the time-tagged spectral sequence for region 2. It is seen that the energy flux remains steady during the first 400 s, with variations less than 10%. After 400 s, it rapidly decreases until the end of the observation, to $\sim$7 mW m^{-2}, a decrease by a factor of 7. The CR (Figure 5f) continuously decreases with a nearly constant slope, from $\sim$30 to $\sim$3. As seen in Figure 5g, the large CR values suggest high mean energies of the precipitating electrons, ranging from $\sim$365 to $\sim$75 keV. During the 400 first seconds, the stable values of the energy flux combined with the drop of CR (i.e., of the mean energy) suggests that (at least) two different populations of electrons account for the observations. A part of the electrons building the current flow seems to be very energetic at the beginning of the sequence. As the electron energy decreases, the total number of electrons remains constant, meaning that the acceleration potential decreases as the flow of electrons remains constant or that the population source changed during the sequence. In a theoretical point of view, it means that the source density goes up as the current density goes up, keeping $W_{\parallel}$ roughly constant. The current density shown in Figure 5h varies from $\sim$0.19 to 0.07 μA m^{-2}, with a maximum at the middle of the exposure.

3.5.3. Region 3

[24] The time-tagged sequence for region 3 is displayed in Figure 5i. The energy flux increases from $\sim$60 to $\sim$107 mW m^{-2} during the first 200 s and then decreases at the same rate until 570 s. The slope then decreases until the end of the sequence. The CR exhibits a similar trend, but it reaches its maximum value after 80 s, i.e., 160 s before the intensity peak. The CR then decreases continuously and stabilizes during the last 100 s. The mean energy curve has the same shape as the CR, with a maximum value of $\sim$544 keV. From the start of the observation until 500 s, the mean energy exhibits the highest values ever recorded, e.g., higher than the previous maximum value of $\sim$250 keV, obtained for only a few auroral spectra we analyzed before (in any region of auroral emission). This behavior, where the mean energy maximizes before the energy flux, was also noticed in previous analyses of the main oval time variations [*Gustin et al.*, 2004]. It may be interpreted in two different ways. First, if the time-tag variations reflect intrinsic changes on the planet, the observations suggest that the most energetic electrons are precipitated first, followed by a larger number of less energetic electrons. This assumption agrees with the hypothesis of a current related to an ''event'' characterized by (at least) two different electron populations, where electrons from one population reach the planet a few seconds before the other (owing to its larger temperature source and/or to a lower density source in the magnetosphere equatorial plane). The time lag between the energy flux's peak and the mean energy's peak may also reflect temporal changes of the characteristics of a single population source during the observation. On the other hand, if the time variations are due to a drift of the features captured by the STIS slit, the comparison between the energy flux and the mean energy reveals that the electron beam is not uniform and produces auroral features that are spatially inhomogeneous. The associated current density shows rather large variations, from $\sim$0.05 μA m^{-2} to $\sim$0.23 μA m^{-2}. As for region 2, these values are in the high range of current densities derived from previous studies of auroral main oval spectra.

3.5.4. Region 4

[25] The energy flux of region 4, shown in Figure 5m, exhibits fairly constant values during the first 120 s and then rapidly decreases from $\sim$67 mW m^{-2} to $\sim$20 mW m^{-2} in 200 s. The slope then decreases and the energy flux reaches $\sim$3 mW m^{-2} at the end of the exposure. The averaged spectrum of region 4 displayed in Figure 3 was obtained from the first 200 s of the exposure, in order to study the most intense part of the auroral sequence. The CR seen in Figure 5n does not show variations as large as those of the energy flux. It varies from $\sim$6 to 3.7 during the first 400 s and then shows more rapid changes, which are affected by a low signal-to-noise ratio, due to the low count number in the detector during the second half of the time sequence. The time variation of the mean energy shows values from 95 to

Figure 5. (a) Time variation of the electron energy flux averaged over 20 s segments and smoothed over 3 data points, for region 1. The left hand side part of the dashed vertical lines shows the time window chosen to extract the spectra. (b) Corresponding CR, (c) variation of the mean electron energy obtained from the CR, (d) precipitated electron current. (e)–(h) Same as Figures 5a–5d for region 2. (i)–(l) Same as Figures 5a–5d for region 3. (m)–(p) Same as Figures 5a–5d for region 4.

155 keV, which are in the range of energies derived from previous spectral studies. The first 300 s of Figure 5p shows the highest values ever recorded for the current density, from $\sim$0.02 μA m^{-2} to $\sim$0.58 μA m^{-2}.

4. Theoretical Considerations

[26] In this section we finally consider the origins of the bright dawn auroras, as indicated by relevant theory. As indicated in section 1, it is generally considered that the auroral emissions associated with the main oval are produced by precipitating middle magnetosphere electrons that are accelerated along the field lines into the ionosphere in regions of upward directed field-aligned current [e.g., *Cowley and Bunce*, 2001; *Hill*, 2001; *Southwood and Kivelson*, 2001; *Nichols and Cowley*, 2004]. Field-aligned acceleration is required because the warm magnetospheric electrons that form the particle source for such currents are sufficiently tenuous that the maximum current that they can carry without acceleration falls far short of that required by the magnetosphere-ionosphere coupling current circuit. For example, *Scudder et al.* [1981] using Voyager data reported that the warm middle magnetosphere electrons have energies of 2–3 keV and densities typically in the range $\sim 10^3$–10^4 m^{-3}. The maximum current that can be carried by this population without acceleration, corresponding to a full downward going loss cone and an empty upward going loss cone, is then in the range $\sim$0.001–0.01 μA m^{-2}, compared with typical field-aligned currents required by the dynamics (and the auroral observations) of $\sim$0.1–0.3 μA m^{-2}. As a consequence, the magnetospheric electrons must be accelerated by field-aligned potentials into the ionosphere to produce the required currents, increasing their energies typically to $\sim$50–150 keV in the process, as deduced from HST spectra by *Gustin et al.* [2004]. The precipitating energy fluxes of the electrons are thereby also strongly increased, from $\sim$0.01 to 0.1 mW m^{-2} for the unaccelerated population, to a few tens of mW m^{-2} for the accelerated population, sufficient to produce an (unabsorbed) main oval aurora of a few hundred kR.

[27] Here we will assume that the same basic process also applies to the bright dawn auroras, in which the above results indicate that the precipitating electrons are occasionally accelerated to energies up to $\sim$550 keV. This assumption remains plausible in the jovian context even at such extreme energies, since *Nichols and Cowley* [2005] and *Cowley et al.* [2005] have shown that the cross-field potential across the outer and middle magnetosphere is $\sim$10 MV, a factor of twenty times larger than the peak field-aligned potentials considered here. Physically, in terms of this theory, the observation of unusually high auroral electron energies and bright auroras in the dawn region implies either that the upward current densities out of the main oval are unusually intense (perhaps due to an unusually intense shear in the plasma flow), or that the properties of the source plasma have altered such that the maximum current that can be carried by the unaccelerated population is reduced (perhaps due to a reduction in electron density), or both. The observations discussed in the last section, combined with relevant theory, allow these possibilities to be investigated. The applicable theory used here is basically *Knight*'s [1973] kinetic theory of auroral electron acceleration by quasi-static field-aligned electric fields, as employed previously by *Gustin et al.* [2004]. However, electrons of a few hundred keV have energies that are a significant fraction of their rest energy ($\sim$511 keV) and should therefore be treated relativistically. Here we therefore employ the relativistic generalization of *Knight*'s [1973] theory recently developed for this purpose by *Cowley* [2006] and begin by outlining the relevant results.

[28] It is first assumed that the source electrons have an isotropic Maxwellian distribution function corresponding to number density N_o and thermal energy kT. The maximum upward current density that can be carried to the ionosphere by these electrons without field-aligned acceleration is then

$$j_{\parallel o} = \frac{eN_o c}{2} \frac{\left(\frac{mc^2}{kT} + 1\right)}{\left(\frac{mc^2}{kT}\right)^2 \exp\left(\frac{mc^2}{kT}\right) \mathrm{K}_2\left(\frac{mc^2}{kT}\right)} \approx eN_o \left(\frac{kT}{2\pi m}\right)^{1/2}, \quad (1)$$

where e and m are the electron charge and rest mass, respectively, c is the speed of light, and K_2 is the modified Bessel function of the second kind of order 2. The second form on the RHS of equation (1) is an approximation valid when $kT \ll mc^2$, such that (as here) the source distribution is nonrelativistic. When the required field-aligned current density above the ionosphere, $j_\parallel$, exceeds $j_{\parallel o}$, the electrons must be accelerated along the field lines into the ionosphere. The minimum field-aligned voltage Φ required to produce current density $j_\parallel$ is given by the solution of

$$\left(\frac{j_\parallel}{j_{\parallel o}}\right) = 1 + \left(\frac{e\Phi}{kT}\right) + \frac{1}{2} \frac{\left(\frac{e\Phi}{kT}\right)^2}{\left(\frac{mc^2}{kT} + 1\right)}, \quad (2)$$

where we refer to *Cowley* [2006] for further details. The last term on the right-hand side of equation (2) may be neglected for nonrelativistic accelerations (i.e., for $e\Phi \ll mc^2$). In the latter case, equation (2) then reduces to the nonrelativistic result obtained by *Knight* [1973]. The corresponding field-aligned kinetic energy flux of the accelerated electrons is

$$\left(\frac{W_\parallel}{W_{\parallel o}}\right) = 1 + \left(\frac{e\Phi}{kT}\right) + \frac{1}{2}\left(\frac{e\Phi}{kT}\right)^2 + \frac{1}{2} \frac{\left(\frac{e\Phi}{kT}\right)^3}{\left(2\frac{mc^2}{kT} + 3\right)}, \quad (3)$$

where $W_{\parallel o}$ is field-aligned kinetic energy flux of the unaccelerated source electrons, given by

$$W_{\parallel o} = \frac{N_o kTc}{2} \frac{\left(2\frac{mc^2}{kT} + 3\right)}{\left(\frac{mc^2}{kT}\right)^2 \exp\left(\frac{mc^2}{kT}\right) \mathrm{K}_2\left(\frac{mc^2}{kT}\right)} \approx 2N_o kT \left(\frac{kT}{2\pi m}\right)^{1/2}. \quad (4)$$

Again, the nonrelativistic expression for $W_\parallel$, first obtained by *Lundin and Sandahl* [1978], corresponds to equation (3) with the last term omitted, while the approximate form in equation (4) is again valid for a nonrelativistic source population. We can also obtain the average kinetic energy of the precipitating electrons, $\langle E \rangle$, by dividing equation (3) by equation (2) to obtain

$$\langle E \rangle = \frac{eW_\parallel}{j_\parallel} = kT \frac{\left(\left(2\frac{mc^2}{kT} + 3\right)\left(1 + \left(\frac{e\Phi}{kT}\right) + \frac{1}{2}\left(\frac{e\Phi}{kT}\right)^2\right) + \frac{1}{2}\left(\frac{e\Phi}{kT}\right)^3\right)}{\left(\left(\frac{mc^2}{kT} + 1\right)\left(1 + \left(\frac{e\Phi}{kT}\right)\right) + \frac{1}{2}\left(\frac{e\Phi}{kT}\right)^2\right)}. \quad (5)$$

Clearly, if nonrelativistic electrons are accelerated through a potential drop $e\Phi$ which is much larger than their initial thermal energy kT, as here, then equation (5) simply becomes $\langle E \rangle \approx e\Phi$.

[29] We now apply this theory to the results obtained in the previous section, for simplicity specifically to the averaged quantities in Table 2. We recall that the physical quantities derived from the HST observations are the average kinetic energy $\langle E \rangle$ of the precipitating electrons from the color ratio (in four spatial windows), and the precipitating electron energy flux from the auroral brightness. From these quantities the electron current density can then be immediately obtained from their quotient, as in the previous section. Assuming that the source electrons have an initial energy $kT = 2.5$ keV as determined from Voyager data by *Scudder et al.* [1981], and as used in the previous analyses cited above, we can then determine the accelerating potential energy from equation (5), and the source number density from either equations (2) or (3). The values obtained are shown in the final two columns of Table 2. As anticipated above, the solution of equation (5) in the case that $\langle E \rangle \gg kT$ gives values for $e\Phi$ that are just slightly smaller than $\langle E \rangle$, while the source densities lie in the range from $\sim$570 to $\sim 7 \times 10^3$ m^{-3}, thus modestly exceed the range $\sim 10^3$–10^4 m^{-3} quoted by *Scudder et al.* [1981].

[30] In order to set these observations within the context of previous results, the data points derived here from the four spatial windows are shown in Figure 6b by numbered dots in a plot of energy flux versus current density. The results obtained by *Gustin et al.* [2004] from 23 more typical spectral observations are shown by crosses. The solid lines show the relationship expected from the above theory (equations (1)–(4)) for fixed source plasma parameters, with $kT = 2.5$ keV, and $N_o = 10^4$ m^{-3} (lower line) and 10^3 m^{-3} (upper line), these values thus corresponding to the electron energy and density range reported by *Scudder et al.* [1981]. The relativistic formulae given above have been used throughout, though the differences relative to *Knight*'s [1973] nonrelativistic theory only become significant for mean particle kinetic energies above $\sim$100 keV, approaching the rest energy. Lines of constant average electron energy are shown by the sloping dotted lines, corresponding to 50, 100, 200, and 400 keV from the lower to the upper line in the plot. It can be seen that the values derived previously are generally confined between the two theoretical curves as reported by *Gustin et al.* [2004], with energy fluxes peaking at $\sim$30 mW m^{-2}, current densities at $\sim$0.4 μA m^{-2}, and with average energies in the range $\sim$50–200 keV. It can be seen that the point from region 1 lies essentially within this group, with a moderate current density and low energy flux, corresponding to a fairly high plasma source density ($\sim 4.8 \times 10^3$ m^{-3}) and consequent low accelerating potential ($\sim$54 kV) and averaged electron energy. The points from regions 2 and 3, however, lie outside of this group, with unusually high values of the energy flux, particularly for region 3, associated with modestly high values of the current density. These points therefore imply a low source density, of $\sim 8.8 \times 10^2$ and $\sim 5.7 \times 10^2$ m^{-3} for regions 2 and 3 respectively, and a correspondingly high value of the accelerating potential ($\sim$277 and $\sim$460 kV, respectively) and precipitating electron energy. Finally, the point for region 4 also lies well outside the group of previously determined points, corresponding to large values of both the energy flux and current density. This point then corresponds to a relatively high value of the source density ($\sim 6.9 \times 10^3$ m^{-3}), which limits the accelerating voltage to $\sim$117 kV despite the very high value of the current.

[31] It can thus be seen that differing conditions prevail in the two branches of the bright dawn auroras seen in Figure 4. In the poleward branch extending to earlier local times observed in Regions 2 and 3, the current density is only modestly high, well within the usual range previously determined, but the aurora is unusually bright because the source density is low, requiring strong acceleration of the auroral electrons to hundreds of keV energy. In the equatorward branch, however, mapping to smaller equatorial radial distances, the density is in the upper range of usual values, but the aurora is bright because the current flowing, required by the dynamics, is unusually intense, such that the electrons are accelerated to energies of $\sim$117 keV despite the large density. Both scenarios mentioned above for the production of bright auroras, low densities and large currents, are therefore involved in separate regions in the present event.

5. Summary

[32] An exceptionally bright Jovian aurora has been observed with STIS during a HST orbit on 21 September 1999, both in the imaging and spectral modes. The auroral maximum brightness was observed on the main oval morning arc, peaking at $\sim$1.8 MR, that is almost four times the main oval brightness previously observed during normal conditions. The images obtained at the start and at the end of the HST orbit (separated by 37 min) were used to characterize the spatial evolution of the bright arc. It is seen that the emission is located on the reference oval, with a leading edge nearly fixed in λ_{III} longitudes and a trailing edge extending 20° in the nightside. The auroral oval separates in two arcs, as also observed in a few other STIS observations. An equatorward bright spot is also observed nearly corotating, reaching a maximum brightness of $\sim$500 kR.

[33] The spatially resolved spectral observation of the HST orbit permitted us to extract four spectra, corresponding to four spatial regions on the planet. The spatial zones, labeled from 1 to 4, correspond to the poleward to the equatorward portions of the arc, respectively. The spectra have a spectral resolution of $\sim$4.8 Å and cover the FUV from 1100 to 1700 Å. The spectral brightness was used to derive the energy flux of the precipitating electrons while the color ratio, which is a measure of the attenuation of H_2's auroral emission by hydrocarbons (mainly methane), was used to deduce the mean energy of the primary electrons. On the basis of the 1-D model atmosphere described by *Grodent et al.* [2001], a CR–mean energy relationship was built in order to estimate the electron's mean energy. The characteristics of the morning arc may be summarized as follows:

[34] Spectra 1 and 4 have mean CR of 1.9 and 4.9, corresponding to mean electron energies of $\sim$55 and $\sim$120 keV, which are in the range of previous values obtained from STIS and GHRS observations. Spectra 2 and 3 reveal unusually high color ratios (18.5 and 45.5),

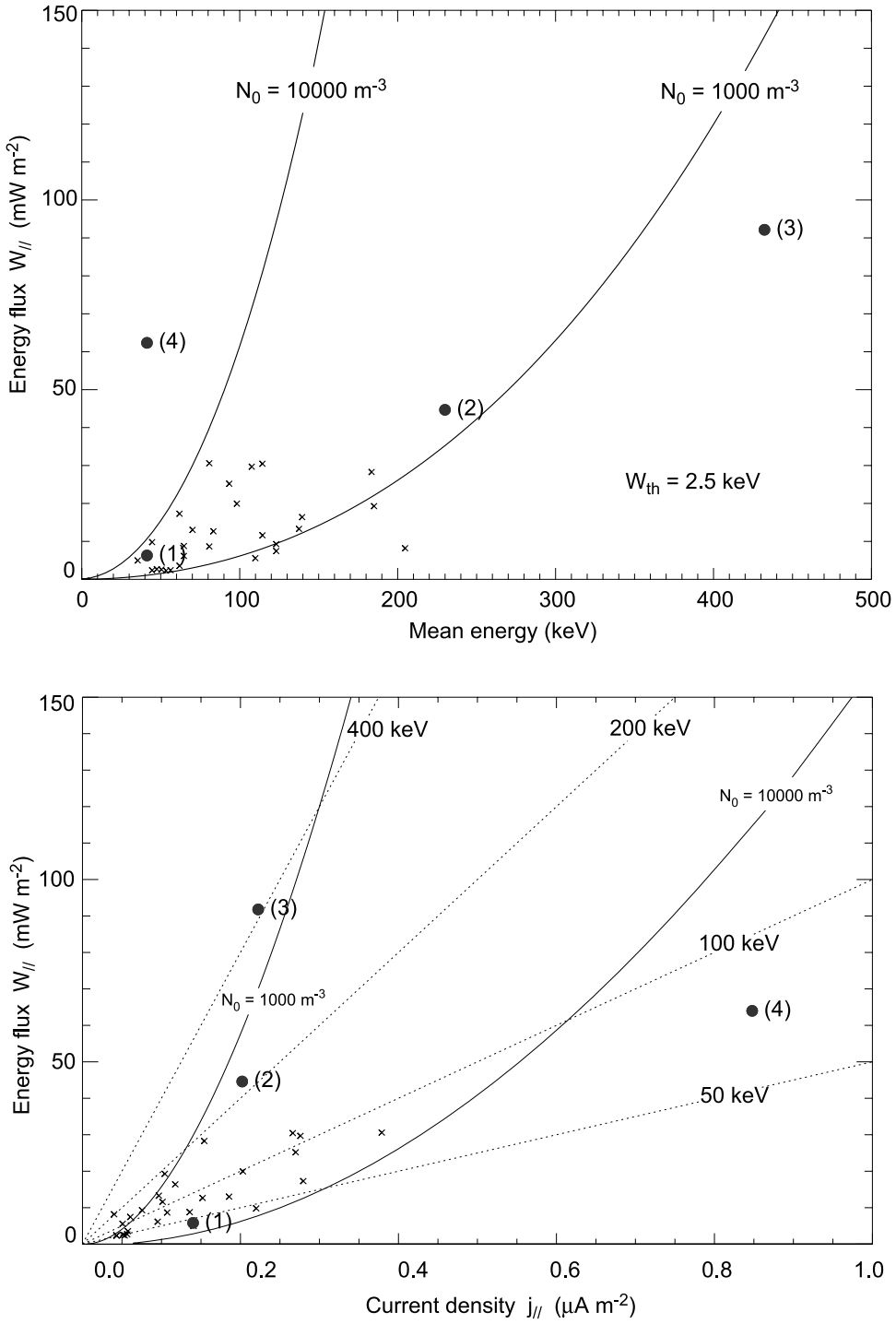

Figure 6. (a) Relationship between the mean energy of the precipitated electrons at the top of the atmosphere and the electron energy flux for the morning arc observation. The four dots correspond to the average values obtained from the four extracted spectra. These observations are compared with theoretical relativistic curves based on *Knight*'s [1973] kinetic theory of field aligned currents. The crosses show the energy flux and acceleration potential obtained from previous main oval spectra analyzed by *Gustin et al.* [2004]. (b) Plot of the energy flux versus current density. The sloping dotted lines show the variations of energy flux with the current density, assuming constant average energies of 50, 100, 200, and 400 keV.

leading to mean electron energies of ~280 and ~460 keV. Furthermore, the mean current densities of spectra 1 to 3 lie in the range ~0.09–0.2 $\mu A\ m^{-2}$, compatible with those expected on the basis of previous analyses of spectral data and from theoretical models. Owing to the high-energy flux and relatively low mean energy of the primary electrons producing spectrum 4, its mean current density is 0.54 $\mu A\ m^{-2}$, outside the maximum value 0.4 $\mu A\ m^{-2}$ recorded in previous analysis of STIS auroral spectra [*Gustin et al.*, 2004].

[35] The properties of the precipitating electrons obtained from the spectra have been compared with theoretical expectations based on *Knight*'s [1973] kinetic theory of field-aligned electric field acceleration associated with field-aligned currents. Owing to the electron's acceleration that is a significant fraction of their rest energy in case of spectra 2 and 3, a relativistic generalization of *Knight*'s [1973] theory developed by *Cowley* [2006] was employed. Assuming a magnetospheric source electron population with a thermal energy of 2.5 keV, it is seen that spectra 1 and 4 are compatible with electron densities of 1×10^3 and $1 \times 10^4\ m^{-3}$, as presented by *Scudder et al.* [1981] from Voyager measurements in Jovian's magnetospheric equatorial plane. Spectra 2 and 3 are characterized by slightly lower electron source densities, namely 880 and 570 m^{-3}, respectively.

[36] Temporal variations of the electron's energy fluxes and mean energies were examined from the time-tagged spectra. The largest variations were observed in the case of spectrum 3, with energy fluxes varying from ~10 to ~110 mW m^{-2} and mean energies varying from ~140 to ~545 keV. The main trend of the data is a covariation of the energy flux and electron's mean energy but that cannot be interpreted as a near-steady magnetosphere-ionosphere coupling current system.

[37] **Acknowledgments.** This work is based on observations with the NASA/ESA Hubble Space Telescope, obtained at the Space Telescope Science Institute (STScI), which is operated by the AURA, Inc. for NASA. JCG and DG acknowledge support from the Belgian Fund for Scientific Research (FNRS), SWHC from PPARC grant PPA/G/0/2003/00013, and JTC from NASA STScI grant HST-GO-100140.01-A to Boston University. Funding for this research was also provided by the PRODEX program of the European Space Agency.

[38] Wolfgang Baumjohann thanks W. R. Pryor and another reviewer for their assistance in evaluating this paper.

References

Ballester, G. E., and the WFPC 2 Science Team (1996), Time-resolved observations of Jupiter's far-ultraviolet aurora, *Science*, *274*, 409.

Broadfoot, A. L., et al. (1979), Extreme ultraviolet observations from Voyager 1 encounter with Jupiter, *Science*, *204*, 979.

Clarke, J. T., and the WFPC 2 Science Team (1996), Far-UV imaging of Jupiter's aurora with HST/WFPC 2, *Science*, *274*, 404.

Clarke, J. T., et al. (1998), Hubble Space Telescope imaging of Jupiter's UV aurora during the Galileo orbiter mission, *J. Geophys. Res.*, *103*, 20,217.

Clarke, J. T., et al. (2002), Ultraviolet Auroral Emissions from the magnetic footprints of Io, Ganymede, and Europa on Jupiter, *Nature*, *415*, 997.

Connerney, J. E. P. (1992), Doing more with Jupiter's magnetic field, in *Planetary Radio Emissions III*, Austrian Acad. of Sci. Press, Vienna.

Connerney, J. E. P., M. H. Acuna, N. F. Ness, and T. Satoh (1998), New models of Jupiter's magnetic field constrained by the Io flux tube footprint, *J. Geophys. Res.*, *103*, 11,929.

Cowley, S. W. H. (2006), Current-voltage and kinetic energy flux relations for relativistic field-aligned acceleration of auroral electrons, *Ann. Geophys.*, *24*, 325–338.

Cowley, S. W. H., and E. J. Bunce (2001), Origin of the main auroral oval in Jupiter's coupled magnetosphere-ionosphere system, *Planet. Space Sci.*, *49*, 1067.

Cowley, S. W. H., I. I. Alexeev, E. S. Belenkaya, E. J. Bunce, C. E. Cottis, V. V. Kalegaev, J. D. Nichols, R. Prangé, and F. J. Wilson (2005), A simple axi-symmetric model of magnetosphere-ionosphere coupling currents in Jupiter's polar ionosphere, *J. Geophys. Res.*, *110*, A11209, doi:10.1029/2005JA011237.

Dols, V., J.-C. Gérard, J. T. Clarke, J. Gustin, and D. Grodent (2000), Diagnostics of the Jovian aurora deduced from ultraviolet spectroscopy: Model and GHRS observations, *Icarus*, *147*, 251.

Gérard, J.-C., V. Dols, R. Prangé, and F. Paresce (1994), The morphology of the north Jovian ultraviolet aurora observed with the Hubble Space Telescope, *Planet. Space Sci.*, *42*, 905.

Gérard, J.-C., J. Gustin, D. Grodent, P. Delamere, and J. T. Clarke (2002), The excitation of the FUV Io tail on Jupiter: Characterization of the electron precipitation, *J. Geophys. Res.*, *107*(A11), 1394, doi:10.1029/2002JA009410.

Gérard, J.-C., J. Gustin, D. Grodent, and J. T. Clarke (2003), Spectral observations of transient features in the FUV Jovian polar aurora, *J. Geophys. Res.*, *108*(A8), 1319, doi:10.1029/2003JA009901.

Gladstone, G. R., M. Allen, and Y. L. Yung (1996), Hydrocarbon photochemistry in the upper atmosphere of Jupiter, *Icarus*, *119*, 1.

Grodent, D., J. H. Waite Jr., and J.-C. Gérard (2001), A self-consistent model of the Jovian auroral thermal structure, *J. Geophys. Res.*, *106*, 12,933.

Grodent, D., J. T. Clarke, J. H. Waite, J. Kim, and S. W. H. Cowley (2003a), Jupiter's main auroral oval observed with HST-STIS, *J. Geophys. Res.*, *108*(A11), 1389, doi:10.1029/2003JA009921.

Grodent, D., J. T. Clarke, J. H. Waite, S. W. H. Cowley, J.-C. Gérard, and J. Kim (2003b), Jupiter's polar auroral emissions, *J. Geophys. Res.*, *108*(A10), 1366, doi:10.1029/2003JA010017.

Grodent, D., J.-C. Gérard, J. Gustin, B. H. Mauk, J. E. P. Connerney, and J. T. Clarke (2006), Europa's FUV auroral tail on Jupiter, *Geophys. Res. Lett.*, *33*, L06201, doi:10.1029/2005GL025487.

Gustin, J., D. Grodent, J.-C. Gérard, and J. T. Clarke (2002), Spatially resolved far ultraviolet spectroscopy of the Jovian aurora, *Icarus*, *157*, 91.

Gustin, J., J.- C. Gérard, D. Grodent, S. W. H. Cowley, J. T. Clarke, and A. Grard (2004), Energy–flux relationship in the FUV Jovian aurora deduced from HST-STIS spectral observations, *J. Geophys. Res.*, *109*, A10205, doi:10.1029/2003JA010365.

Hill, T. W. (1979), Inertial limit on corotation, *J. Geophys. Res.*, *84*, 6554.

Hill, T. W. (1980), Corotation lag in Jupiter's magnetosphere: Comparison of observation and theory, *Science*, *207*, 301.

Hill, T. W. (2001), The Jovian auroral oval, *J. Geophys. Res.*, *106*, 8101.

Knight, S. (1973), Parallel electric fields, *Planet. Space Sci.*, *21*, 741.

Lundin, R., and I. Sandahl (1978), Some characteristics of the parallel electric field acceleration of electrons over discrete auroral arcs as observed from two rocket flights, *Eur. Space Agency Spec. Publ.*, *ESA SP-135*.

Nichols, J. D., and S. W. H. Cowley (2004), Magnetosphere-ionosphere coupling currents in Jupiter's middle magnetosphere: Effect of precipitation-induced enhancement of the ionospheric Pedersen conductivity, *Ann. Geophys.*, *22*, 1799.

Nichols, J. D., and S. W. H. Cowley (2005), Magnetosphere-ionosphere coupling currents in Jupiter's middle magnetosphere: Effect of magnetosphere-ionosphere decoupling by field-aligned auroral voltages, *Ann. Geophys.*, *23*, 799.

Prangé, R., D. Rego, L. Pallier, J. E. P. Connerney, P. Zarka, and J. Queinnec (1998), Detailed study of FUV Jovian features with the post-COSTAR HST faint object camera, *J. Geophys. Res.*, *103*, 20,195.

Scudder, J. D., E. C. Sittler Jr., and H. S. Bridge (1981), A survey of the plasma electron environment of Jupiter: A view from Voyager, *J. Geophys. Res.*, *86*, 8157.

Southwood, D. J., and M. G. Kivelson (2001), A new perspective concerning the influence of the solar wind on the Jovian magnetosphere, *J. Geophys. Res.*, *106*, 6123.

Waite, J. H., Jr., et al. (2001), An auroral flare at Jupiter, *Nature*, *410*, 787.

Yung, Y. L., G. R. Gladstone, K. M. Chang, J. M. Ajello, and S. K. Srivastava (1982), H_2 fluorescence spectrum from 1200 to 1700 Å by electron impact: Laboratory study and application to jovian aurora, *Astrophys. J.*, *254*, L65.

J. T. Clarke, Center for Space Physics, Boston University, Boston, MA 02215, USA.

S. W. H. Cowley, Department of Physics and Astronomy, University of Leicester, Leicester, LE1 7RH, UK.

J.-C. Gérard, D. Grodent, and J. Gustin, Laboratoire de Physique Atmospherique et Planetaire, Universite de Liege, Liege, Belgium. (j.gustin@ulg.ac.be)

G. R. Gladstone, Space Science and Engineering Department, Southwest Research Institute, P. O. Box 28510, San Antonio, TX 78228, USA. (randy.gladstone@swri.org)